PHYSICAL REVIEW B **70**, 155418 (2004)

Coordination dependence of hyperfine interactions at impurities on fcc metal surfaces.
I. Electric-field gradient

S. Cottenier,[1,*] V. Bellini,[2,†] M. Çakmak,[1,3] F. Manghi,[2] and M. Rots[1]
[1]*Instituut voor Kern- en Stralingsfysica, Katholieke Universiteit Leuven, Celestijnenlaan 200 D, B-3001 Leuven, Belgium*
[2]*INFM-National Research Center on nanoStructures and bioSystems at Surfaces, (S3) and Dipartimento di Fisica,*
Università di Modena e Reggio Emila, Via Campi 213/A, I-41100 Modena, Italy
[3]*Department of Physics, Gazi University, Teknikokullar, TR-06500 Ankara, Turkey*
(Received 10 December 2003; revised manuscript received 24 May 2004; published 29 October 2004)

We present a comparison between accurate *ab initio* calculations and a high-quality experimental data set (1986–2002) of electric-field gradients of Cd at different sites on Ni, Cu, Pd, and Ag surfaces. Experiments found a systematic rule to assign surface sites on (100) and (111) surfaces based on the main component of the electric-field gradient, a rule that does not work for (110) surfaces. Our calculations show that this particular rule is a manifestation of a more general underlying systematic behavior. When looked upon from this point of view, (100), (111) *and* (110) surfaces behave in precisely the same way. The physical mechanism behind the systematics of the EFG for other 5*sp* impurities (Cd-Ba) at different fcc surfaces sites is revealed, showing in a natural way why the first half of the 5*p* elements shows a coordination dependence that is opposite with respect to the second half.

DOI: 10.1103/PhysRevB.70.155418 PACS number(s): 68.47.De, 68.35.Fx, 68.35.Dv, 75.70.Rf

I. INTRODUCTION

Nuclear probe techniques, such as Mössbauer spectroscopy, Perturbed Angular Correlation spectroscopy (PAC), Nuclear Magnetic Resonance (NMR), and others, have proven in the past to be versatile tools for the study of a broad set of phenomena. By simultaneously detecting both electric-field gradients (EFG) and magnetic hyperfine fields (HFF), it is possible to obtain a fingerprint of the electronic and magnetic configuration near and at the probe nucleus.[1–6] *Ab-initio* band structure calculations have assumed an important role in supporting, improving or confuting the interpretation of experimental data. Especially for such sensitive properties as HFF's or EFG's, the availability of these parameter-free calculations with an accuracy that is comparable with the experimental error bars, has opened new possibilities. For instance, by a combination of experiments and calculations, the systematics of the EFG in pure 3*d* and 4*d* hcp-metals[7] and of 5*sp* impurities in noncubic metals (Zn, Cd, Sb) could be understood (Refs. 8 and 9, and references therein). A similar mechanism was revealed for the EFG on X in RX_3 compounds (R = lanthanide, $X = Rh \rightarrow Xe$).[10]

In a series of two papers (the second paper is published as Ref. 11), we turn our attention to electric-field gradients and magnetic hyperfine fields of isolated impurity atoms at fcc metal surfaces. Many experimental data are available for the EFG of Cd at several sites on various fcc metal surfaces (see Table I). From these data, commonly accepted guidelines for the site identification of Cd on (100) and (111) metal surfaces were derived, while the (110) surface seemed to behave differently. A first goal of this paper is to demonstrate that these guidelines are a manifestation of a simple and general coordination dependence mechanism that is valid for *all* low-index surfaces (Sec. III). A second goal is to check whether the mechanism for the systematics of the EFG throughout the series of 5*sp* impurities that was established previously for elemental transition metals[8] and lanthanide compounds[10] is valid also at surfaces. The second paper[11] of this series will deal with several questions in which the magnetic hyperfine field of impurities at surfaces is involved.

Our work on the EFG at surfaces follows pioneering cluster calculations by Lindgren *et al.*,[12–15] who investigated HFF and EFG of Cd as an adatom or in a terrace site at various Ni, Cu, Pd, and Ag surfaces.

II. METHOD AND DETAILS OF THE CALCULATIONS

For the present calculations we have employed state of the art first-principles techniques, developed within the Density Functional Theory (DFT).[16–18] Most of the calculations have been performed using the full-potential augmented plane wave + local orbitals (APW+lo) method[19,20,18] as implemented in the WIEN2k package.[21] We have simulated the surface+impurity complexes by using the slab-supercell approach. The impurities have been put both in an adatom site and at a substitutional position in the surface layer (called the terrace site from now on) at the three low-Miller-index surfaces, which in turn were composed of repeated slabs of 5 to 7 substrate layers (up to 11 for test calculations), separated by some vacuum space. The size and shape of the cells were chosen such as to avoid an artificial interaction between the impurity atoms. For symmetry reasons, the impurity atoms were placed at both sides of the slabs. Test calculations showed that about 6 Å of vacuum (equivalent to about 3.5 atomic layers) is sufficient to decouple the Cd atoms at the two surfaces, and that a similar distance is needed to decouple the Ni atoms within the same plane. More details of the slabs and the vacuum are given in tables later in the paper and in the following paper (Ref. 11). As an exchange-correlation functional, the PBE generalized gradient approximation (GGA)[22] was used. A few test calculations (see later) have been performed with the local density approximation

1098-0121/2004/70(15)/155418(10)/$22.50

(LDA). In the APW+lo method, wave functions, charge density, and potential are expanded in spherical harmonics within nonoverlapping atomic spheres of radius R_{MT} and in plane waves in the remaining space of the unit cell. R_{MT} values of 2.2 a.u. for Ni and Cu, and 2.4 a.u. for the Pd, Ag, and all 5*sp* impurities were chosen throughout. The maximum ℓ for the waves inside the atomic spheres was confined to $\ell_{max}=10$. For the majority of the cases, the wave functions in the interstitial region were expanded in plane waves with a cutoff of $K_{max}=7.0/R_{MT}^{min}=3.18$ a.u.$^{-1}$ or better, while the charge density was Fourier expanded up to $G_{max}=16\sqrt{\mathrm{Ry}}$. For the Brillouin zone sampling, a mesh of special k points corresponding to at least a $14\times14\times14$ mesh (104 points) for bulk fcc Ni was taken. The lattice constant of Ni used throughout the calculations is the one which minimizes the GGA bulk total energy, i.e., $a_{Ni}^{GGA}=3.51$ Å. For Cu, Pd, and Ag, the experimental lattice constants were used.

When the perfect crystal structure is broken, as in the presence of an impurity, atomic relaxations of the atoms in the vicinity of impurity appear. Such relaxations have a rather long range character, and lead to a volume change of the crystal, as testified by refined lattice parameter measurements. Additionally, since they alter the nature and strength of bonds, they change local properties such as the EFG as well. Atomic relaxations tend to be larger in size the more open the crystal structure (e.g., zinc blend),[23] but it has been shown in the literature to be very important also in close-packed matrices.[24] As taking into account atomic relaxations is computationally quite expensive, we have sped up the calculations by using a combination of methods. First, the atomic positions were relaxed using the pseudopotential plane wave VASP code.[25,26] The all-electron APW+lo code was then used in a second stage to further relax the atoms to their equilibrium positions (with forces less than 1 mRy/a.u.), and to calculate the EFG. The expected error bar on the EFG values is smaller than $\pm2\times10^{21}\mathrm{V/m}^2$ (see for instance Ref. 27).

III. ELECTRIC-FIELD GRADIENT AT CD

For an efficient discussion later in this section, we first summarize a few properties and conventions with respect to the electric-field gradient (EFG) at a nucleus in a crystal (for a more elaborate discussion, see, for instance, Refs. 28 and 29). The EFG is a traceless, symmetric tensor of rank 2 (5 components), and is a measure of the deviation from spherical symmetry of the electronic charge density around the nucleus under consideration. In its principal axis system (PAS), the EFG tensor is diagonal with diagonal elements V_{xx}, V_{yy}, and V_{zz} and $V_{xx}+V_{yy}+V_{zz}=0$ (traceless; hence specifying 2 out of the 3 quantities is enough). The axes of the PAS are conventionally labeled such that $|V_{zz}|\geqslant|V_{yy}|\geqslant|V_{xx}|$. Instead of specifying 2 of the 3 diagonal elements, usually the couple (V_{zz},η) is specified, with η the so-called asymmetry parameter which equals $(V_{xx}-V_{yy})/V_{zz}$ $(0\leqslant\eta\leqslant1)$. Often one refers with the term "electric-field gradient" to V_{zz} only. Whenever we use the word "EFG," we mean the tensor with its 5 components. If we mean the main component in the PAS, we write V_{zz}.

TABLE I. Experimental absolute values of the principal component $|V_{zz}|$ of the electric-field gradient tensor of Cd at various metallic surfaces, with references tracked down as much as possible to the original sources. Units: 10^{21} V/m^2. A quadrupole moment of 0.83 barn[30] was used to extract V_{zz} from the measured quadrupole interaction frequency. The lowest available measurement temperatures were chosen, and are specified below (0 K if a reliable extrapolation was available).

	Ni	Cu	Pd	Ag
(100) terrace	8.2 [a,b]	10.3 [c]	8.2 [d]	7.5 [e]
(100) adatom	2.8 [f] / 0.3 [g]	0.8 [h]	2.8 [i]	0.3 [j]
(110) terrace	–	7.9 [k]	7.9 [l]	7.0 [m]
(110) adatom	–	–	8.5 [n]	–
(111) terrace	11.5 [o] / 12.3 [p]	10.2 [q]	10.2 [r]	8.6 [s]
(111) adatom	1.0 [t]	–	0.4 [u]	–

[a] Unpublished Ref. 31, mentioned in Refs. 14 and 6.
[b] Reference 6, $T=270-300$ K.
[c] Reference 28, $T=0$ K.
[d] Reference 32, $\eta=0.16$ (!), $T=0$ K.
[e] Reference 33, $T=0$ K.
[f] Unpublished Ref. 31, mentioned in Ref. 14.
[g] Unpublished Ref. 31, mentioned in Ref. 34.
[h] Mentioned in Ref. 13: private communication from G. Schatz.
[i] Reference 32, $T=77$ K.
[j] Reference35, $T=77$ K.
[k] Reference 36, $\eta=0.74$, $T=0$ K.
[l] Unpublished Ref. 37, mentioned in Ref. 15. $\eta=0.97$.
[m] Reference 33, $\eta=0.80$, $T=77$ K.
[n] Unpublished Ref. 37, mentioned in Ref. 15. $\eta=0.42$.
[o] References 5, $T=0$ K.
[p] Reference34, $T=340$ K.
[q] Reference 38 and 36, $T=0$ K.
[r] Reference 39 and 29, $T=0$ K.
[s] Reference 33, $T=0$ K.
[t] Reference 34, $T=36$ K.
[u] References 39 and 29, $T=77$ K.

Over the past two decades, a large body of experimental results has been obtained for the EFG's of Cd at different surfaces of Ni, Cu, Pd, and Ag (see Table I for a summary of the experimental work, with references tracked down as much as possible to the original sources). In contrast to what the structure of Table I might suggest, the assignment of the experimental values to either terrace or adatom sites does not happen in a direct way. For (100) and (111) surfaces, it is easy to separate terrace and adatom sites from all other ones (steps, kinks) due to the axial symmetry $(\eta=0)$ of the EFG and the perpendicular orientation of the *z*-axis of its PAS. It is much harder to deduce which of both is the terrace site and which one is the adatom site. Only for a few cases a thorough experimental analysis has been performed: Ag(100)[35] and Pd(111).[29,39] Arguments include the thermal annealing behavior, the fraction of different sites dependent on the type of vicinal cut, and not at least a comparison with early *ab initio* cluster calculations.[12,13] Apart from these two well-tested cases, the partial information from thermal annealing behavior only [Cu(111)[36]] or from agreement with cluster calculations only [Cu(100)[36]] further supports the assignment in Table I. To our knowledge, the results on Pd(110) are published only recently and in an indirect way (unpublished Ref. 37, mentioned in Ref. 15). Prior to this information, Table I was commonly summarized by the following practical "rule:" *on a metal surface, a large V_{zz} for Cd indicates the terrace site, while a small V_{zz} indicates the adatom site*. This rule has practical applications: if for a not yet studied surface a large (small) V_{zz} is measured, this will be taken as evidence for the fact that Cd is at the terrace (adatom) site. This was what was done, e.g., by Potzger *et al.*[34] to assign the adatom and terrace sites on Ni(100) and Ni(111), in a study of the coordination dependence of the HFF of Cd at Ni surfaces. If the rule would not be universal, this site assignment could be wrong, and consequently also their conclusion on the parabolic coordination number dependence of the Cd-HFF (see the second paper[11] of this series for a further discussion). Therefore, we will first examine the validity of this rule. Is it really valid for all (100) and (111) surfaces of the nonmagnetic metals Cu, Pd, and Ag (i.e., also for the cases that are not experimentally tested in detail)? Can the rule be transferred without changes to the magnetic metal Ni? And is it really true only for (100) and (111) surfaces, and not for (110) (as the recent Pd information suggests)? Finally, what is the physical mechanism that lies behind this rule?

In response to these questions, we present in Table II(a) the calculated V_{zz} for both relaxed and unrelaxed Ni surfaces, together with their assigned experimental values (taken from Table I). We did not find in the literature any experimental investigation for Cd at the Ni(110) surface. Instead, for a qualitative comparison, the data for Cd at the Pd(110) surface are enclosed in parentheses in Table II(a). We also include the results obtained with the cluster method by Lindgren.[15] Unfortunately, the cluster calculations of Lindgren spanned all the orientations only for the Cu surface, while for Cd on Ni only the terrace sites at Ni(100) and (111) surfaces have been simulated. Results for Cu and Pd surfaces are therefore included in Table II(a) in parentheses as well. We recall here that different to the cluster results of Lindgren, our calculations are for bulk slabs and not for nonperiodic clusters. Moreover we do a "full" relaxation of all the atomic positions in the cell, while due to insufficient accuracy of the method, no real forces have been calculated by Lindgren: the distance between Cd and the surface was fixed at the experimental distance, and the surrounding Ni atoms were kept in their ideal *fcc* positions (in contrast to this, the Cd atom in our *un*relaxed calculations was at an ideal *fcc* lattice site). Our fully relaxed results compare generally very well with the experiments, predicting for (100) and (111) a low V_{zz} (close to zero) for all adatom sites, and a considerably higher V_{zz} for the terrace site, in compliance with the experimental rule. For the (110) surface, terrace and adatom sites have a comparable V_{zz}, again in agreement with the experimental observation. Taking into account the rather different approximations, there is also reasonable agreement between our unrelaxed slab calculations and the unrelaxed cluster results, the former being generally closer to experiment [especially for (111)]. For the (110)-surface, the EFG is not axially symmetric ($\eta \neq 0$). Values for η are included in Table II(a) as well. Relaxation can be seen to have a moderate influence on η, and the considerably larger η in terrace sites as seen in experiments, is well-reproduced. A direct comparison with experimental values for η is difficult with the present data set, however [no experiments for Ni(110) and no relaxed calculations for Pd(100)]. More details on the nature of the relaxations are discussed in Ref. 11 (Sec. III-1 and Table II).

TABLE II. All calculations refer to a slab with 7 substrate layers. About 13 Å vacuum was used for the terrace sites, about 9.5 Å vacuum for the adatom sites. (a) Column 1: unrelaxed slab calculations for V_{zz} of Cd on Ni surfaces. Column 2: idem, but relaxed (see Sec. III and Table II of Ref. 11 for more details on the relaxation). Column 3: unrelaxed cluster calculations for V_{zz} of Cd on Ni surfaces, when available. If no values were available, results for Cu or Pd surfaces are given instead. Column 4: the absolute value of the experimental V_{zz} for Cd on Ni surfaces, if available (if not, values for a Pd surface are given). (b) Relaxed slab calculations for V_{zz} of Cd in terrace and adatom sites at one magnetic and three nonmagnetic (100) surfaces (sign included), compared with the absolute value of the corresponding experimental V_{zz}. See Sec. III-1 and Table II of Ref. 11 for more details on the relaxation. Units: $10^{21}\ \mathrm{V/m^2}$ everywhere.

(a)

	APW+lo Unrelax.	APW+lo Relax.	Cluster calc. Ref. 15	|Exp.| see Table I
(100) Terrace	10.5	8.6	11.0	8.2
(100) Adatom	4.0	1.9	$(-0.8)_{\mathrm{Cu}}$	2.8/0.3
(110) Terrace	9.5	−9.7	$(11.2)_{\mathrm{Pd}}$	$(7.9)_{\mathrm{Pd}}$
(110) Adatom	−9.3	−6.4	$(-8.3)_{\mathrm{Pd}}$	$(8.5)_{\mathrm{Pd}}$
(111) Terrace	10.8	13.0	16.5	11.5/12.3
(111) Adatom	−1.4	−2.9	$(-6.2)_{\mathrm{Cu}}$	1.0
(110) Terrace	$\eta=0.83$	$\eta=0.74$	$\eta_{\mathrm{Pd}}=0.97$	$\eta_{\mathrm{Pd}}=0.97$
(110) Adatom	$\eta=0.18$	$\eta=0.23$	$\eta_{\mathrm{Pd}}=0.28$	$\eta_{\mathrm{Pd}}=0.42$

(b)

	(100) terrace APW+lo	(100) terrace |Exp.|	(100) adatom APW+lo	(100) adatom |Exp.|
Ni	8.6	8.2	1.9	2.8/0.3
Cu	9.9	10.3	−2.0	0.8
Pd	9.1	8.2	3.4	2.8
Ag	8.5	7.5	0.4	0.3

For the (110) terrace site we observe a change in the sign of V_{zz}, when moving from the unrelaxed to the relaxed system. This is readily explained as follows. V_{zz} is defined as the

TABLE III. The three calculated ($V_{\mathrm{ii}}^{\mathrm{calc}}$, unrelaxed) and experimental ($V_{\mathrm{ii}}^{\mathrm{exp}}$, see Table I for references) components of EFG tensor in its PAS for Cd at 6 Pd surface, sites, ordered according to the number of nearest neighbors for Cd (NN). Similar slabs as in Table II used. Units: 10^{21} V/m^2. The usual convention for labeling the axes of the PAS is *not* followed: the z-axis is perpendicular to the surface, x-and y-axes are in the surface plane. For (100) and (111) surfaces all directions in the surface plane are equivalent for the EFG. For the (110) surface, our x-axis refers to the $[1\overline{1}0]$ direction, and our y-axis to the [001] direction. The principal component—which would be labeled V_{zz} in the usual convention—is printed in boldface. The sign of the experimental values was not measured, but is chosen here to agree with the calculations (for the small numbers for NN=3, this is nothing more than a guess). The number Cd−5p electrons split into n_{px}^{calc}, n_{py}^{calc}, and n_{pz}^{calc} is given as well.

	♯NN	$V_{\mathrm{xx}}^{\mathrm{calc}}$	$V_{\mathrm{yy}}^{\mathrm{calc}}$	$V_{\mathrm{zz}}^{\mathrm{calc}}$	$V_{\mathrm{xx}}^{\mathrm{exp}}$	$V_{\mathrm{yy}}^{\mathrm{exp}}$	$V_{\mathrm{zz}}^{\mathrm{exp}}$	$n_{p_x}^{\mathrm{calc}}$	$n_{p_y}^{\mathrm{calc}}$	$n_{p_z}^{\mathrm{calc}}$
(111) terrace	9	−4.8	−4.8	**9.6**	−5.1	−5.1	**10.2**	0.1478	0.1478	0.0952
(100) terrace	8	−4.4	−4.4	**8.8**	−4.1	−4.1	**8.2**	0.1321	0.1321	0.0876
(110) terrace	7	−7.6	−0.5	**8.1**	−7.8	−0.1	**7.9**	0.1330	0.1054	0.0799
(110) adatom	5	2.0	**−6.2**	4.2	−2.5	−6.0	**8.5**	0.0685	0.0984	0.0664
(100) adatom	4	−1.4	−1.4	**2.8**	−1.4	−1.4	**2.8**	0.0645	0.0645	0.0580
(111) adatom	3	0.4	0.4	**−0.8**	0.2	0.2	**−0.4**	0.0425	0.0425	0.0576

largest component of the electric field gradient tensor in its principal axis system. But it might happen that there are two components of similar size, that have then necessarily opposite signs and yield a large asymmetry parameter η (=close to 1). This is exactly what we found for the (110) terrace case. There is a large positive component along the normal on the (110) surface, while an almost as large negative component exists along the $[1\overline{1}0]$ direction in the (110) plane. Upon relaxation the latter negative component becomes in absolute value larger than the positive one, and the latter axis becomes the one along which V_{zz} is defined. Experiments on the Pd(100) surface show instead the EFG z-axis for the terrace site to lay along the normal to the (110) plane. The calculated component of the EFG along this direction is $+8.4\times10^{21}$ V/m^2 for the relaxed Ni-surface. It is this value which should be compared to the experimental 7.9×10^{21} V/m^2 for the Pd(110) terrace site. In the relaxed Ni(100) adatom case, the z-axis is the [001] direction in the (110) plane while experiments on Pd(110) find again the [110] direction. The component of the calculated EFG along the latter direction is $+3.9\times10^{21}$ V/m^2 for Ni(110). This deviates considerably from the experimental value for Pd, but is in good agreement with the unrelaxed Pd-calculations to be discussed in Table III. We suspect that there is a problem with the experiment here. For the other two substrate orientations, (100) and (111), the asymmetry parameter η is zero and there is therefore no doubt on which component is the largest one: we find in all cases the principal axis along the surface normal, as in the experiment.

Having verified that the practical site assignment rule is valid for magnetic Ni(100) and Ni(111) surfaces, and not for Ni(110), we now examine for one type of surface — (100) — whether other elemental metal substrates show the same behavior. Table II(b) shows the calculated and experimental V_{zz} at the (100) surfaces of Ni, Cu, Pd and Ag. The calculations are in very satisfying agreement with the experiments, and it is safe now to conclude that the EFG in all of these 24 surface sites behaves in the same way.

Finally, we search for the physical mechanism that is responsible for this systematic behavior. Instead of considering for this the Ni-calculations from Table II, we calculated the EFG of Cd at a complete set of unrelaxed Pd-surfaces. This avoids the complication of an EFG coming from spin-up and spin-down electrons, and it allows for a more direct comparison with experiment because for Pd all six cases are measured (Table I). It is not harmful not to consider relaxation here, because now we are looking for a global mechanism, not for fine details. The results are given for every diagonal component of the EFG separately in Table III, together with the corresponding experimental components (mind the unconventional labeling of the axes, as specified in the caption of Table III). Considering the fact that these are unrelaxed calculations, they reflect the experimental trend very well and hence these Pd-surfaces form a reliable model system to search for the physical mechanism.

Already in the very first successful *ab initio* calculations of EFG's in metals, it has been shown that the magnitude and sign of the principal component V_{zz} are reflected in the so-called asymmetry count Δn_p of the p-electrons (for Cd, the completely filled d-shell does not contribute to the EFG). The asymmetry count is defined as $\Delta n_p=\frac{1}{2}(n_{p_x}+n_{p_y})-n_{p_z}$, with n_{p_i} the number of electrons in the p_i-orbital (see Ref. 7 for the first analysis, and, e.g., Refs. 10, 40–42 for applications): spherical symmetry $(n_{p_x}=n_{p_y}=n_{p_z})$ leads to $\Delta n_p=0$ (hence $V_{\mathrm{zz}}=0$), charge accumulation along the z-axis (n_{p_z} large) leads to $\Delta n_p<0$ (hence $V_{\mathrm{zz}}<0$), etc. For our analysis, we slightly extend this idea and take as a working hypothesis that the sign and magnitude of *any* diagonal component V_{ii} are reflected in a *generalized* asymmetry count $\Delta n_p^i=\frac{1}{2}(n_{p_j}+n_{p_k})-n_{p_i}$ (and cyclic permutations). This hypothesis is checked by Fig. 1(a), where the calculated V_{ii} from Table III (right scale) are compared with the asymmetry counts Δn_p^i derived from the calculated number of p electrons in Table III (left scale). With the right choice of scales in Fig. 1(a), the Δn_p^i and V_{ii} data points almost coincide, which means that apart from a unique scaling factor both quantities reflect ba-

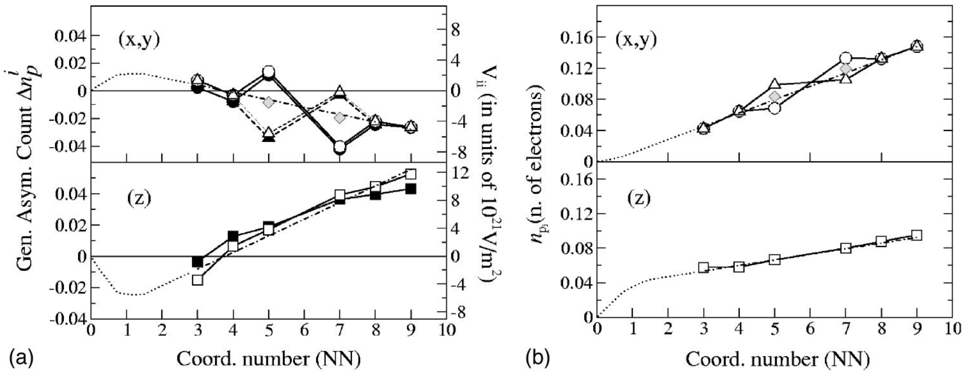

FIG. 1. (a) Black symbols: calculated components of the Cd EFG on Pd (see Table III, black symbols refer to the right scale). White symbols: generalized asymmetry counts (see the text), calculated from the n_{p_i} in Table III (white symbols refer to the left scale). Gray symbols [for (110) surfaces only]: the average of Δn_p^x and Δn_p^y, which would be the value of $\Delta n_p^x = \Delta n_p^y$ in the hypothetical case of axial symmetry ($\eta = 0$). Circles, triangles, and squares are relative to the *x*,*y*,*z* components, respectively, of the plotted quantities. Dotted-dashed lines: Δn_p^i obtained from the least squares fit in Fig. 1(b). The dotted lines are calculated using the extrapolation of Fig. 1(b). (b) The n_{p_i} from Table III. Gray symbols [for (110) surfaces only]: the average of n_{p_x} and n_{p_y} in the hypothetical case of axial symmetry ($\eta = 0$). Dotted-dashed lines: least squares fit, with tentative extrapolation (dotted line) to NN=0 (free atom). Both in (a) and (b) the data for the *xy*-plane and for the *z*-direction are displayed separately for clarity.

sically the same behavior. This proves our working hypothesis: the observed behavior of all components of the EFG is nothing more than a manifestation of the properties of the distribution of the Cd 5*p*-electrons over the *x*-, *y*- and *z*-directions. Hence, if we understand the behavior of the n_{p_i} in Table III, we understand the EFG. This greatly facilitates our search, as—in contrast to the V_{ii}— the n_{p_i} have a direct and intuitively understandable relation to the chemical bonds between Cd and its Pd neighbors.

The coordination dependence of the n_{p_i} is visualized in Fig. 1(b), together with a least squares fit. The picture is complicated a bit by the fact that n_{p_x} and n_{p_y} are not identical to each other for (110) surfaces. To make the discussion more transparent, we will therefore first assume a hypothetical (110) surface with axial symmetry ($\eta = 0$) for which $n_{p_x} = n_{p_y}$ (gray symbols in Fig. 1; they are the average of the calculated n_{p_x} and n_{p_y}). We now clearly see an almost linear dependence of n_{p_x} (or n_{p_y}) and n_{p_z} on NN [least squares fit in Fig. 1(b)]: both $n_{p_x}(n_{p_y})$ and n_{p_z} decrease linearly while reducing the coordination, the decrease being stronger for $n_{p_x}(n_{p_y})$ than for n_{p_z}. If we calculate the Δn_p^i corresponding to the least squares fits in Fig. 1(b), we obtain the straight lines in Fig. 1(a) [for overall axial symmetry, gray symbols for NN=(5,7)]: this proves that the two-slope model from Fig. 1(b) is indeed the key responsible for the observed behavior of the EFG. A simple mechanism explains why these slopes must be different. Obviously, n_{p_i} should decrease with decreasing NN: Cd has no native 5*p*-electrons, hence in the free atom limit (NN=0) all n_{p_i} should be zero. The reason why $n_{p_x}(n_{p_y})$ gets reduced faster upon decreasing NN than n_{p_z}, can be understood from the difference between the horizontal and vertical coordination of Cd. The low-coordination adatom sites have no neighbors in the XY-plane, and hence $n_{p_x}(n_{p_y})$ quickly becomes zero. There are always, however, substrate atoms underneath Cd, i.e., in the *Z*-direction, whereas Cd is in a terrace or an adatom site. Therefore n_{p_z} has a tendency to stay more constant. This is exactly what is observed in Fig. 1(b). Up to now we artificially kept $\eta = 0$ for the (110)-surface. Reintroducing $\eta \neq 0$ in our discussion only redistributes the charges within the horizontal plane, and therefore does not affect the above conclusion.

An alternative and complementary way to visualize the evolution of the *p*-electrons and V_{zz} as a function of coordination for Cd on Pd is provided by the *p*-anisotropy function[10,41,42] (Figs. 2 and 3). This is a function of energy—just as the Density Of States (DOS)—that gives the integrated value of the previously defined asymmetry count $\Delta n_p = \frac{1}{2}(n_{p_x} + n_{p_y}) - n_{p_z}$ up to that energy. The value of this function at the Fermi energy gives the actual *p*-asymmetries as given, e.g., in Table III. If this function is negative at a given energy E_0, it means that for the *p*-states in the interval $[-\infty, E_0]$ the p_z-states outweigh p_x and p_y. The *p*-anisotropy function was used before[7,43] to explain the positive V_{zz} for Cd in hcp-Cd, as is sketched in Fig. 3(a): shorter interatomic distances in the *XY*-plane make the p_{xy}-band broader than the p_z-band, such that in the lower half of the *p*-band the *p*-anisotropy—and hence V_{zz}—is negative. Cd is at the bottom of the 5*p*-band, and is therefore expected to have a negative V_{zz}. For Cd on Pd-surfaces, the *p*-anisotropy functions given in Fig. 2 start with a characteristic negative contribution near −4 eV, which is very similar to what was calculated for Cd at a $4/mmm$ site in AuCu$_3$-type lattices.[10] We will demonstrate in Sec. IV that this is due to a hybridization involving the Cd-5*s* and Cd-5p_z electrons (not 5p_{xy}), an effect that was not properly understood before. For low coordination numbers, another strongly negative contribution is present above E_F. When the coordination number increases, this gradually transforms in a strongly positive contribution: first at the lower end near E_F, and extending to over 5 eV above E_F for the highest coordination number. What matters is the value of the anisotropy function at E_F, and this evolves from a small negative value for NN=3 (p_z excess, as there are no horizontal bonds) to strongly positive values for larger NN (p_{xy} excess, as to the surface side a vertical bond is

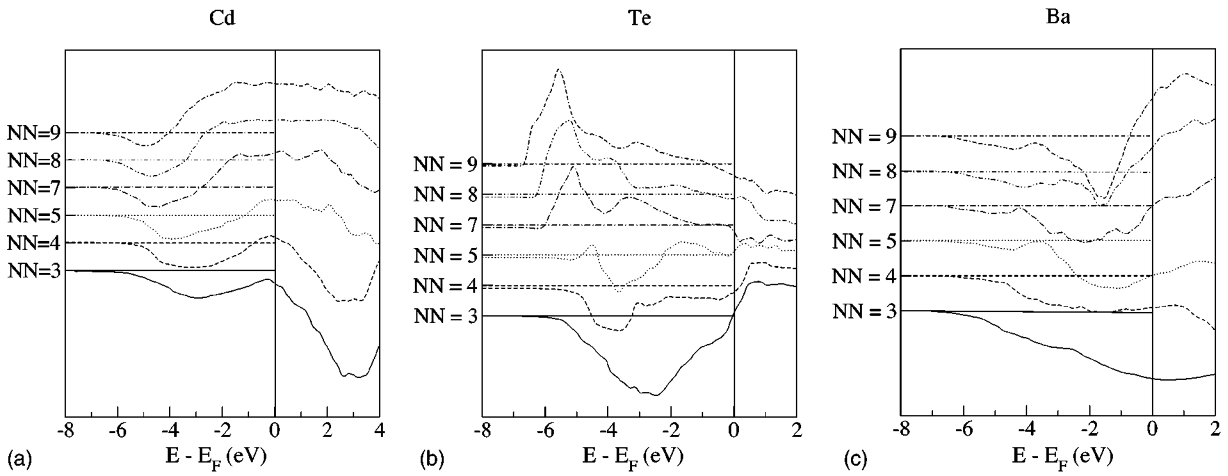

FIG. 2. A *p*-anisotropy function of Cd ($5p$=total), Te ($5p$=total), and Ba ($6p$ only) at sites with different coordination on various Pd surfaces. For clarity, the curves within each plot have been vertically displaced from the $y=0$ axis. The distance between the baseline of neighboring curves is (a) 0.03, (b) 0.08, and (c) 0.02 states/eV, which simultaneously calibrates the three *Y*-axes.

missing). The anisotropy function will play a major role in understanding the systematics of the EFG for other $5p$-impurities in Sec. IV, where more interpretations will be provided on the shape of the *p*-anisotropy function for Cd as well.

We emphasize that for a given coordination number, the *p*-distribution for sure depends on the exact spatial arrangement of the Pd neighbors. The behavior as a function of the coordination number is so smooth only because we are dealing with fairly "similar" environments (Pd underneath, vacuum above). Furthermore, a tentative extrapolation of Fig. 1(b) to very low coordination sites (NN=1, 2) suggests a negative V_{zz} there. This is confirmed for an NN=2 environment for Cd on Ni, where we calculate $V_{zz}=-2.4\times10^{21}$ V/m^2(see Table I of Ref. 11 for the exact geometry of this environment).

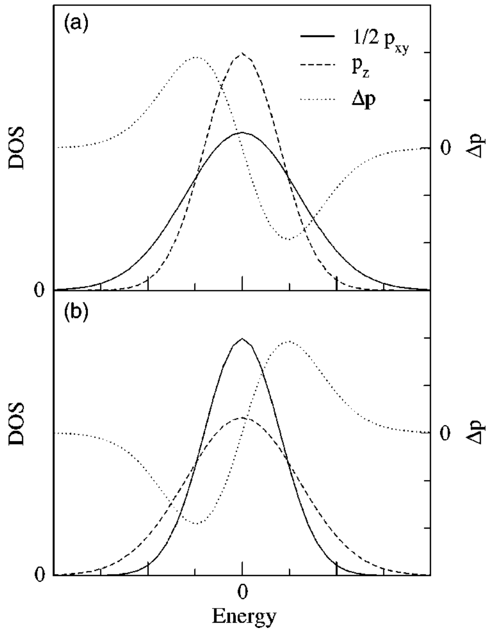

FIG. 3. (a) Left scale: sketch of the Density Of States (DOS) for p_{xy} and p_z states of $5p$ impurities in bulk hcp metals. Right scale: the corresponding *p*-anisotropy curve $\Delta p(E)=\int_{-\infty}^{E}\frac{1}{2}\mathbf{(}n_{p_x}(E')+n_{p_y}(E')\mathbf{)}-n_{p_z}(E')dE'$(picture taken from Refs. 43 and 8). It is demonstrated in Sec. IV that a similar picture applies for $5p$ impurities in terrace sites at fcc metal surfaces. (b) Similar, but now for $5p$ impurities as an adatom on fcc metal surfaces (see Sec. IV).

In contrast to the discrete behavior suggested by the practical rule ("terrace site means large V_{zz}; adatom site means low V_{zz}"), we conclude that there is a continuous evolution as a function of the coordination number. The (100) and (111) terrace sites are both highly coordinated, and therefore have indeed the largest V_{zz}, while the opposite is true for the (100) and (111) adatom sites. The (110) terrace and adatom sites have intermediate coordination—and therefore comparable V_{zz}'s—which is why the "rule" does not seem to work for (110). However, there is nothing exceptional about the (110) surface.

IV. ELECTRIC-FIELD GRADIENT AT OTHER 5*p*-IMPURITIES

Being the last $4d$ transition element, Cd feels an EFG that is nevertheless determined by $5p$ states (Sec. III). We now broaden the scope and examine the EFG at a fcc surface of all 9 elements in the series Cd-Ba. Within this series, the effect of the gradual filling of the $5p$-shell can be studied. In addition, for the late elements of the series, also the $6p$-shell will start to fill and the total EFG will result from a competition between the two distinct contributions. The goal is to examine whether the well-established band-filling mechanism for similar impurities in bulk spd-metals[7–9] and in f-electron compounds[10] still holds for the quite different situation of a surface.

Out of all 54 possible situations [all 9 impurity atoms at all 6 surfaces sites (NN=3,4,5,7,8,9)], we first calculate the EFG for 18 of them: all impurities at the adatom (NN=4) and terrace (NN=8) site of a (100) Pd surface. Again no lattice relaxations are taken into account, as we are searching for global mechanisms and not for details. In Fig. 4, the

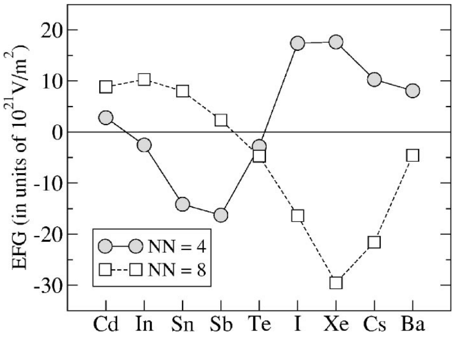

FIG. 4. Calculated V_{zz} for the elements Cd-Ba as an adatom (NN=4) and in a terrace site (NN=8) on an unrelaxed (100) surface of fcc Pd.

calculated values for V_{zz} are given. It can be readily seen from Fig. 4 that the systematics at a surface are different from bulk: for the more bulk-like, highly-coordinated terrace site, the "S-shaped" evolution from positive V_{zz} in the first half of the series to negative values in the second half is very similar to what has been measured and/or calculated for the same series of impurities in bulk spd-metal hosts (Zn, Cd, and Sb; see Refs. 8, 44, and references therein), and bulk *f*-electron compounds.[10] For the less bulk-like, less-coordinated adatom site, however, an *opposite* evolution is seen. Figure 4 suggests that for impurities in the first half of the 5*p*-band the coordination dependence of V_{zz} will be similar to that of Cd (positive values for high coordination, negative values for low coordination), while for the second half of the 5*p* elements the coordination dependence is opposite. In order to find the reason for this difference, we first look at the total *p*-anisotropy curves for all 9 elements in Fig. 5. Additionally, this figure shows the 6*p* anisotropy for Xe, Cs, and Ba as well, put at the bottom of the picture. They can be thought to represent the 5*p* anisotropy of Kr, Rb, and Sr, such that Fig. 5 shows the evolution through all 5*sp* elements, omitting the 4*d* elements (except for Cd). For both sites, the evolution from bottom to top in Fig. 5 can be qualitatively described by a single characteristic curve that gradually shifts to the left and simultaneously gets wrapped up (the development of sharper features). The former effect is due to the filling of the 5*p*-band, while the latter is connected to the flattening of the 5*p*-bands when they get deeper and deeper under the Fermi level. For Xe, Cs, and Ba the *p*-DOS shows very sharp and narrow peaks at 7 or more eV below the Fermi energy. They result in a similarly peaked structure in the *p*-anisotropy. For the terrace site this peak is positive, with a long tail that becomes eventually negative at E_F for the heavier elements. The peak is negative for the adatom site, with a long tail that becomes positive at E_F for the heavier elements. For both sites there is also a negative contribution at the beginning of the *p*-anisotropy. It gradually becomes smaller (=less deep) and becomes horizontal for several eV.

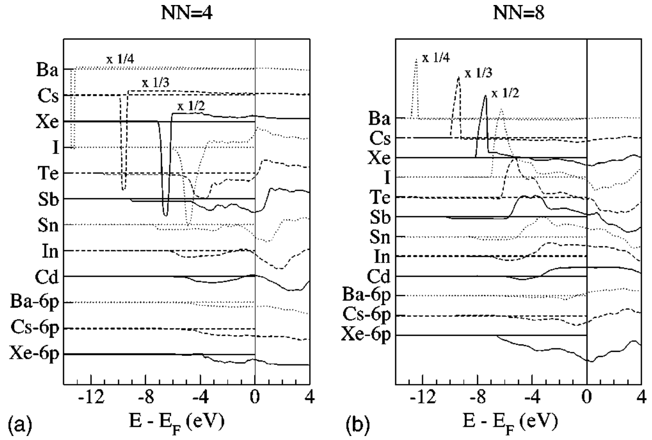

FIG. 5. Total *p*-anisotropy (=5*p*+6*p*) for the elements Cd-Ba as an adatom (NN=4) and in a terrace site (NN=8) on an unrelaxed (100) surface of fcc Pd. For Cd to *I*, a contribution from 6*p*-electrons to the total *p*-anisotropy is negligible, such that their total *p*-anisotropy is a 5*p*-anisotropy. The *p*-anisotropy of Xe, Cs, and Ba has a 5*p* and a 6*p* contribution. Their 6*p*-anisotropy is shown at the bottom of the picture as well (see the text). As for Fig. 2, the curves within each plot have been vertically displaced for clarity. The displacement between neighboring curves is (a) 0.12 and (b) 0.10 states/eV.

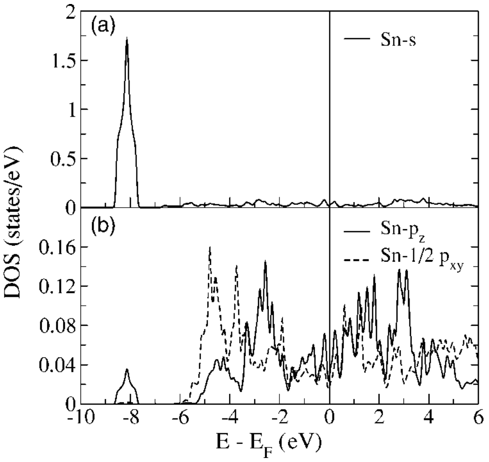

FIG. 6. (a) Partial *s*-DOS for Sn in a terrace site on Pd(100). (b) Partial DOS for $p_{xy}/2$ (full line) and p_z (dashed line) for Sn in a terrace site on Pd(100).

How can all those features be interpreted? (i) The initial negative feature can be identified as due to a 5*s*-5p_z hybridization. Indeed, when going through the series, the 5*s* states of the impurity evolve from a broad peak at or just under E_F to a sharp peak several eV lower (see Fig. 6 for Sn). The hybridization with this 5*s* peak moves some of the 5p_z weight to lower energies, while the 5p_{xy} weight is not affected. This leads to a p_z excess at low energies, and hence to a negative anisotropy function. The deeper in energy the 5*s* states become, the less they can take part in the hybridization —lowering the initial p_z excess, until it effectively vanishes from *I* on. For elements with 6*s* states close to E_F (Xe, Cs, Ba), this effect leads to a shallow negative 6*p*-anisotropy at E_F, and hence a negative V_{zz}^{6p}. (ii) The positive feature that develops into the sharp peak for NN=8 can be understood in the same way as for 5*p* impurities in bulk materials[7–10,43] (see also Sec. III): the bonding in the *XY*-plane is stronger than in the *Z*-direction—an argument that is *a fortiori* true at surfaces because in the positive *Z*-direction there are no

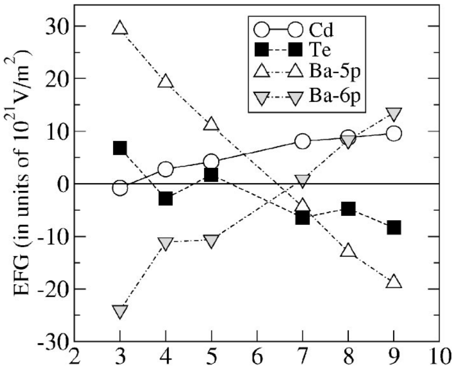

FIG. 7. Coordination dependence of V_{zz} for Cd, Te, and Ba on fcc Pd surfaces. V_{zz} of Ba is split in a $5p$ and a $6p$ contribution.

neighbors – which leads to a p_{xy}-band that is broader than the p_z-band (the latter is clearly visible in Fig. 6, where the main part of the p_{xy}-band starts at −5.8 eV, while p_z starts at −5.2 eV only). This leads to p_{xy}-excess and hence a positive p-anisotropy in the first half of the $5p$-band [Fig. 3(a)], which is what is observed for all elements in Fig. 5(b). An alternative way to formulate this is saying that in the first half of the band bonding states are most populated. Bonding states form the strongest bonds, such that for a terrace site they must be the p_{xy} states. When the same argument is applied to the adatom site, it leads in a natural way to the opposite behavior: bonds are stronger in the Z-direction, as there are no neighbors in the XY-direction for an adatom. The p_z band is broader now (or alternatively the p_z are the bonding states now), which leads to p_z excess and a *negative* p-anisotropy in the first half of the band [Fig. 3(b)]. (iii) In the second half of the p-band, the p-anisotropy becomes negative for the terrace site (and for bulk), which starts to be visible in Fig. 5(b) from Sb on. This indicates p_z excess, which is again due to the smaller p_z-band, or alternatively, to the population of antibonding states [Fig. 3(a)]. The same arguments lead to a positive p-anisotropy for the adatom site [Fig. 3(b)].

This analysis is further confirmed by looking at the p-anisotropy for a single impurity as a function of coordination. The case of Cd was already discussed in Sec. III and Fig. 2(a), where we saw how the p_z excess for low coordination (p_z are bonding states) gradually transforms into a p_{xy} excess for high coordination (p_{xy} are bonding states). What happens in the upper half of the band is not visible for Cd, as this second half lies far above E_F. For Te, however, we can observe both the first and second half of the band [Fig. 2(b)]. The first half of the Te-$5p$ band lies fully under E_F, and transforms from a strongly negative into a strongly positive feature if the coordination increases, just as for Cd. The second half of the band lies at and above E_F, and evolves in the opposite way from positive to negative. Te is simultaneously a warning example of the quantitative limitations of this interpretation: we expect a V_{zz} that changes from positive to negative with increasing coordination. This is certainly the general trend for Te as seen in Fig. 7, but individual environments can deviate from this trend: for the NN=4 environment the V_{zz} is slightly negative instead of positive (while at first sight, looking at Fig. 4, one would have predicted an almost constant coordination dependence for Te). As a last example we show the $6p$-anisotropy for Ba in Fig. 2(c). For low coordination, the negative contribution from the hybridization with the $6s$ states and the negative contribution from the bonding $6p_z$ states cooperate to produce a strongly negative V_{zz}. For high coordination the positive contribution from the bonding $6p_{xy}$ states slightly dominates. As far as the $6p$ states are concerned, Ba is at the beginning of the p-band, and we correctly find an evolution from negative to positive V_{zz}. But for the $5p$ band, Ba is at the end of the band, and the trend must be reversed. This is indeed what is calculated, as shown by Fig. 7. For elements heavier than Ba, the $5p$ states will be at ever more negative energies and will eventually be rigidly spherically symmetric, leading to a zero contribution to V_{zz}. We did not explicitly calculate the coordination dependence of V_{zz} for a Sn impurity, which is experimentally accessible by ^{119}Sn Mössbauer spectroscopy. But by an extrapolation of Fig. 4 it can be expected that adatom and terrace sites on the same surface will lead to almost identical values of V_{zz}, but with a different sign. Because without special care most experiments are insensitive to the sign, this implies that site-identification through V_{zz} of Sn will be difficult in practice.

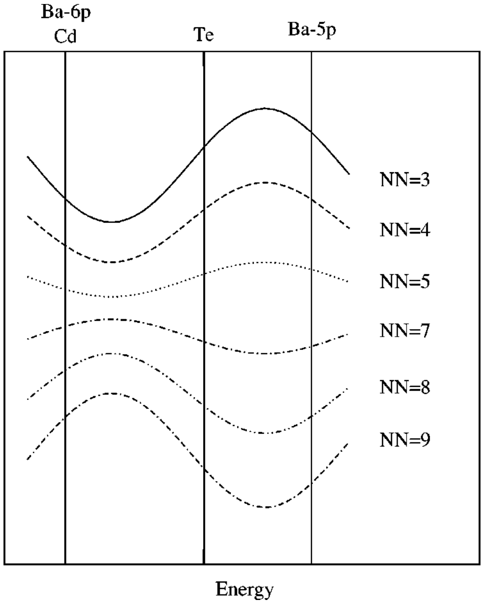

FIG. 8. Qualitative shape of the p-anisotropy for $5p$-impurities on fcc surfaces, varying from high coordination (bottom) to low coordination (top). The trend for a given element can be read by putting the Fermi energy at the appropriate position in the band. Examples are given for the cases shown in Fig. 7. Note that this cartoon does not predict the *magnitude* of V_{zz}, but only the sign and the trend as a function of coordination: due to band narrowing, the p-anisotropy is more peaked near the end of the band, leading to potentially larger values of V_{zz}.

Our analysis can be summarized in the cartoon of Fig. 8, which shows the evolution of the p-anisotropy as a function of coordination. The essential features are present: the evolution from p_z excess to p_{xy} excess with increasing coordination in the first half of the band, and the opposite effect in the second half of the band. In order to find the trend for the coordination dependence of a given impurity, the position of its Fermi energy has to be given. This is indicated on Fig. 8 by vertical lines for the examples that have been discussed.

V. CONCLUSIONS

We have undertaken a comparison of *ab initio* calculations and a high-quality data set—experimentally collected during the past 20 years—of electric-field gradients of Cd at magnetic and nonmagnetic metallic fcc surfaces. We conclude that the experimental practice for (100) and (111) surfaces of assigning a large V_{zz} to terrace sites and a low V_{zz} to adatom sites is correct. However, this "discrete" rule is nothing more than a manifestation of a continuous evolution of the EFG components as a function of the coordination number, an evolution for which we have pointed out the physical mechanism. With this insight, the behavior of the (110) surface is not exceptional at all, in contrast to what the experimental evidence seemed to suggest. As a generalization, we examined the coordination dependence of the electric-field gradient for 9 different elements, spanning the entire 5*p* series. The trend as a function of coordination number is opposite for the first and second half of the 5*p* series, and our analysis reveals the physical mechanism behind this. Having reached these conclusions on the EFG, we can now turn to the magnetic hyperfine field of Cd and other impurities on the magnetic fcc Ni surface, which is the subject of paper II (Ref. 11, the next paper in this issue).

ACKNOWLEDGMENTS

Part of the calculations were performed on computer facilities granted by an INFM project *Iniziativa Trasversale Calcolo Parallelo* at the CINECA supercomputing center. Another part of the computational work was performed on computers in Leuven, in the frame of projects G.0239.03 of the *Fonds voor Wetenschappelijk Onderzoek — Vlaanderen* (FWO), the Concerted Action of the KULeuven (GOA/2004/02) and the Inter-University Attraction Pole (IUAP P5/1). The authors are indebted to L. Verwilst and J. Knudts for their invaluable technical assistance concerning the pc-cluster in Leuven. M. C. thanks the *Onderzoeksfonds* of the KULeuven for financial support (F/02/010).

---

*Electronic address: Stefaan.Cottenier@fys.kuleuven.ac.be
†Electronic address: Bellini.Valerio@unimore.it

[1] R. Vianden, in *Nuclear Physics Application on Materials Science*, edited by E. Recknagel and J. C. Soares (Kluwer Academic, New York, 1988), p. 239.
[2] G. Schatz, in *Nuclear Physics Application on Materials Science*, edited by E. Recknagel and J. C. Soares (Kluwer Academic, New York, 1988), p. 297.
[3] G. Krausch, R. Fink, K. Jacobs, U. Kohl, J. Lohnmüller, B. Luckscheiter, R. Platzer, B.-U. Runge, U. Wöhrmann, and G. Schatz, Hyperfine Interact. **78**, 261 (1993).
[4] H. Haas, Z. Naturforsch. **50a**, 407 (1994).
[5] J. Voigt, R. Fink, G. Krausch, B. Luckscheiter, R. Platzer, U. Wöhrmann, X. L. Ding, and G. Schatz,Phys. Rev. Lett. **64**, 2202 (1990).
[6] H. H. Bertschat, H.-H. Blaschek, H. Granzer, K. Potzger, S. Seeger, W.-D. Zeitz, H. Niehus, A. Burchard, D. Forkel-Wirth, and ISOLDE Collaboration, Phys. Rev. Lett. **80**, 2721 (1998).
[7] P. Blaha, K. Schwarz, and P. H. Dederichs, Phys. Rev. B **37**, 2792 (1988).
[8] H. Haas, Hyperfine Interact. **129**, 493 (2000).
[9] H. Akai, M. Akai, S. Blügel, B. Drittler, H. Ebert, K. Terakura, R. Zeller, and P. H. Dederichs, Prog. Theor. Phys. Suppl. **101**, 11 (1990).
[10] S. J. Asadabadi, S. Cottenier, H. Akbarzadeh, R. Saki, and M. Rots, Phys. Rev. B **66**, 195103 (2002).
[11] V. Bellini, S. Cottenier, M. Çakmak, F. Manghi, and M. Rots, Phys. Rev. B **70**, 155419 (2004).
[12] B. Lindgren, Hyperfine Interact. **34**, 217 (1987).
[13] B. Lindgren, Europhys. Lett. **11**, 555 (1990).
[14] B. Lindgren and A. Ghandour, Hyperfine Interact. **78**, 291 (1993).
[15] B. Lindgren, Z. Naturforsch. **57a**, 544 (2002).
[16] P. Hohenberg and W. Kohn, Phys. Rev. **136**, 864 (1964).
[17] W. Kohn and L. J. Sham, Phys. Rev. **140**, A1133 (1965).
[18] S. Cottenier, "Density Functional Theory and the family of (L)APW-methods: A step-by-step introduction," Instituut voor Kern- en Stralingsfysica, KULeuven, Belgium, 2002, ISBN 90-807215-1-4 (to be found at http://www.wien2k.at/reg_user/textbooks).
[19] E. Sjöstedt, L. Nordström, and D. J. Singh, Solid State Commun. **114**, 15 (2000).
[20] G. K. H. Madsen, P. Blaha, K. Schwarz, E. Sjöstedt, and L. Nordström, Phys. Rev. B **64**, 195134 (2001).
[21] P. Blaha, K. Schwarz, G. Madsen, D. Kvasnicka, and J. Luitz, "WIEN2k, an augmented plane wave + local orbitals program for calculating crystal properties," Karlheinz Schwarz, Techn. Universität Wien, Austria ,1999, ISBN 3-9501031-1-2.
[22] J. P. Perdew, K. Burke, and M. Ernzerhof, Phys. Rev. Lett. **77**, 3865 (1996).
[23] A. Settels, T. Korhonen, N. Papanikolaou, R. Zeller, and P. H. Dederichs, Phys. Rev. Lett. **83**, 4369 (1999).
[24] H. M. Petrilli, P. E. Blöchl, P. Blaha, and K. Schwarz, Phys. Rev. B **57**, 14690 (1998).
[25] G. Kresse and J. Furthmüller, Comput. Mater. Sci. **6**, 15 (1996).
[26] G. Kresse and J. Furthmüller, Phys. Rev. B **54**, 11169 (1996).
[27] P. Dufek, P. Blaha, and K. Schwarz, Phys. Rev. Lett. **75**, 3545 (1995).
[28] T. Klas, J. Voigt, W. Keppner, R. Wesche, and G. Schatz, Phys. Rev. Lett. **57**, 1068 (1986).
[29] E. Hunger and H. Haas, Surf. Sci. **234**, 273 (1990).
[30] K. Herzog, K. Freitag, M. Rauschenbach, and H. Walitzki, Z. Phys. A **294**, 13 (1980).
[31] J. Voigt, Ph.D. thesis, Universität Konstanz, 1990.
[32] R. Fink, B.-U. Runge, K. Jacobs, G. Krausch, J. Lohmüller, B. Luckscheiter, U. Wöhrmann, and G. Schatz, J. Phys.: Condens.

Matter **5**, 3837 (1993).

[33] R. Wesche, R. Fink, T. Klas, G. Krausch, R. Platzer, J. Voigt, and G. Schatz, J. Phys.: Condens. Matter **1**, 7407 (1989).

[34] K. Potzger, A. Weber, H. H. Bertschat, W.-D. Zeitz, and M. Dietrich, Phys. Rev. Lett. **88**, 247201 (2002).

[35] R. Fink, R. Wesche, T. Klas, G. Krausch, R. Platzer, J. Voigt, U. Wöhrmann, and G. Schatz, Surf. Sci. **225**, 331 (1990).

[36] T. Klas, R. Fink, G. Krausch, R. Platzer, J. Voigt, R. Wesche, and G. Schatz, Surf. Sci. **216**, 270 (1989).

[37] G. Filleböck (private communication to B. Lindgren).

[38] T. Klas, R. Fink, G. Krausch, R. Platzer, J. Voigt, R. Wesche, and G. Schatz, Europhys. Lett. **7**, 151 (1988).

[39] E. Hunger, H. Haas, and H. Grawe, Hyperfine Interact. **60**, 999 (1990).

[40] C. Ambrosch-Draxl, P. Blaha, and K. Schwarz, J. Phys.: Condens. Matter **1**, 4491 (1989).

[41] K. Schwarz, C. Ambrosch-Draxl, and P. Blaha, Phys. Rev. B **42**, 2051 (1990).

[42] S. Lany, P. Blaha, J. Hamann, V. Ostheimer, H. Wolf, and T. Wichert, Phys. Rev. B **62**, R2259 (2000).

[43] H. Haas, Z. Naturforsch. A **41**, 78 (1986).

[44] B. Lindgren, Phys. Rev. B **34**, 648 (1986).